Supplementary Materials:

Magnesium as a Novel UV Plasmonic Material for Fluorescence Decay Rate Engineering in Free Solution

Yunshan Wang,[†] Eric M. Peterson,[‡] Joel M. Harris,[‡] Kanagasundar Appusamy,[¶] Sivaraman Guruswamy,[¶] and Steve Blair[*,†]

†*Department of Electrical and Computer Engineering, University of Utah, 50 South Central Campus Drive, Room 3280, Salt Lake City, UT 84112*

‡*Department of Chemistry, University of Utah, 315 South 1400 East, Room 2020, Salt Lake City, UT 84112*

¶*Metallurgical Engineering, University of Utah, Salt Lake City, UT 84112*

E-mail: blair@ece.utah.edu

1 Experimental

1.1 Sample fabrication

We plotted measured top, bottom diameters and undercuts for Mg and Al nanoapertures in fig. S1. Undercuts increase monotonically with dose level, which is the dwell time of ion beam on each aperture. However, top diameters and bottom diameters do not follow the same trend, which can be due to different ion beam focus positions for different apertures. Those dimensions were used in simulation using model (b) in fig3 in the manuscript, to

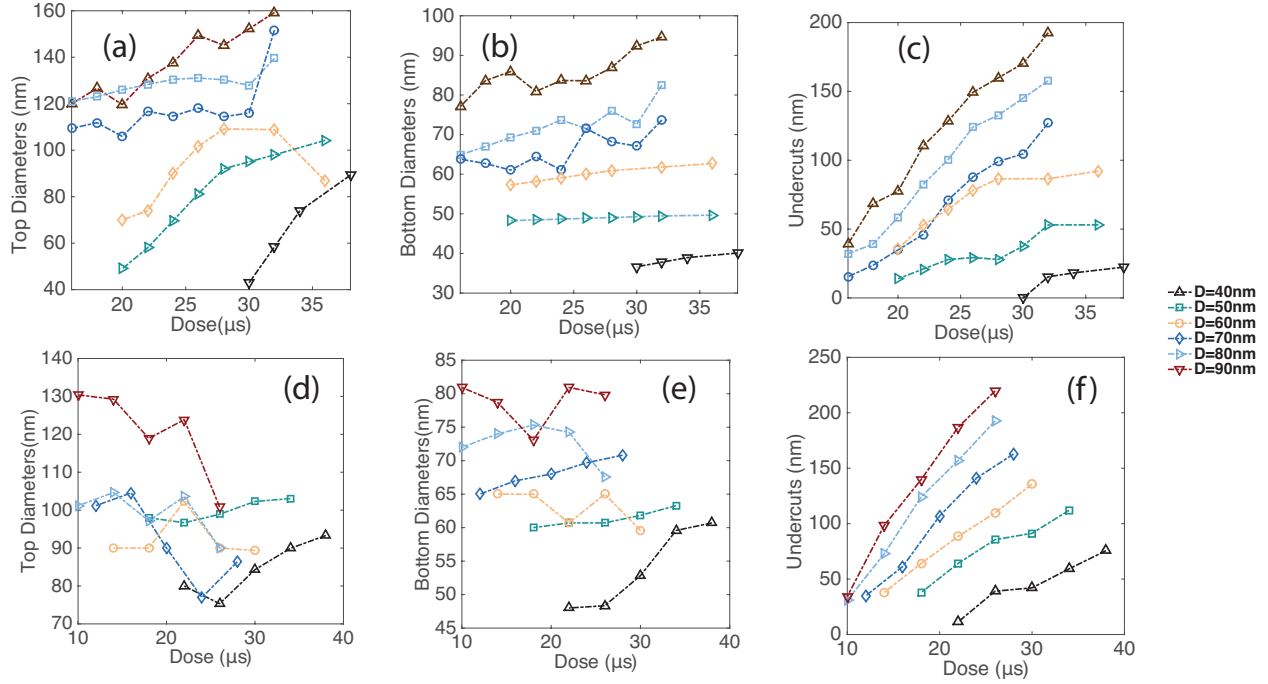compare with experimental data shown in fig.5.

Figure S1: (a) Measured top diameters of Mg nanoapertures versus dose level. (b) Measured bottom diameters of Mg nanoapertures versus dose level. (c) Measured undercuts of Mg nanoapertures versus dose level. (d) Measured top diameters of Al nanoapertures versus dose level. (e) Measured bottom diameters of Al nanoapertures versus dose level. (f) Measured undercuts of Al nanoapertures versus dose level.

Figure.S2(a) shows a cross-section SEM image of Mg nanoaperture with designed diameters 40 nm to 90 nm, from left to right. (b) shows a cross-section SEM image of Al nanoaperture with designed diameters 40 nm and 50 nm. Conical shapes are evident in the SEM images and the dimensions are measured and plotted in fig.S1.

1.2   Fluorescence lifetime setup

Figure.S3 shows an image of lifetime setup. The laser source is a Coherent Chameleon Vision II Ti:Sapphire laser (not shown) which is frequency- tripled using an A·P·E HarmoniXX unit. Routing and beam-shaping optics deliver the 266 nm light to the input of a Picoquant MT-200 system designed specifically for UV operation. A dichroic mirror reflects the input to an Olympus IX 71 inverted microscope with 40X 0.6 NA Ultrafluar UV objective and
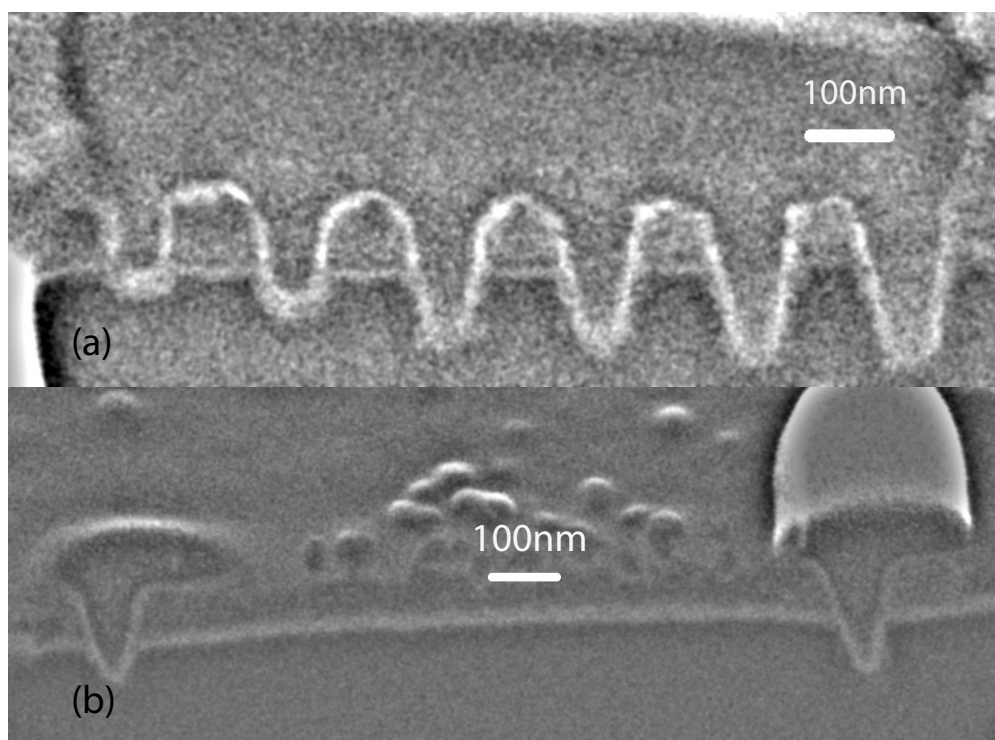
Figure S2: (a) a cross-section SEM image of Mg nanoapertures with designed diameters from 40 nm to 90 nm, from left to right. (b) a cross-section SEM image of Al nanoapertures with designed diameters 40 nm on the left and 50 nm on the right.

nanopositioning stage. Fluorescence collected through the objective passes the dichroic, is confocally imaged onto a 30 μm pinhole, and then passes through a spectral emission filter (357$\pm$22 nm) placed before the UV-sensitive PMT (PMA-C 175-M Ultra). Note that the system has two detection paths, only one of which is used for lifetime measurements. The PMT output is connected to the PicoHarp 300 which records photon arrival time relative to the initial laser pulse.
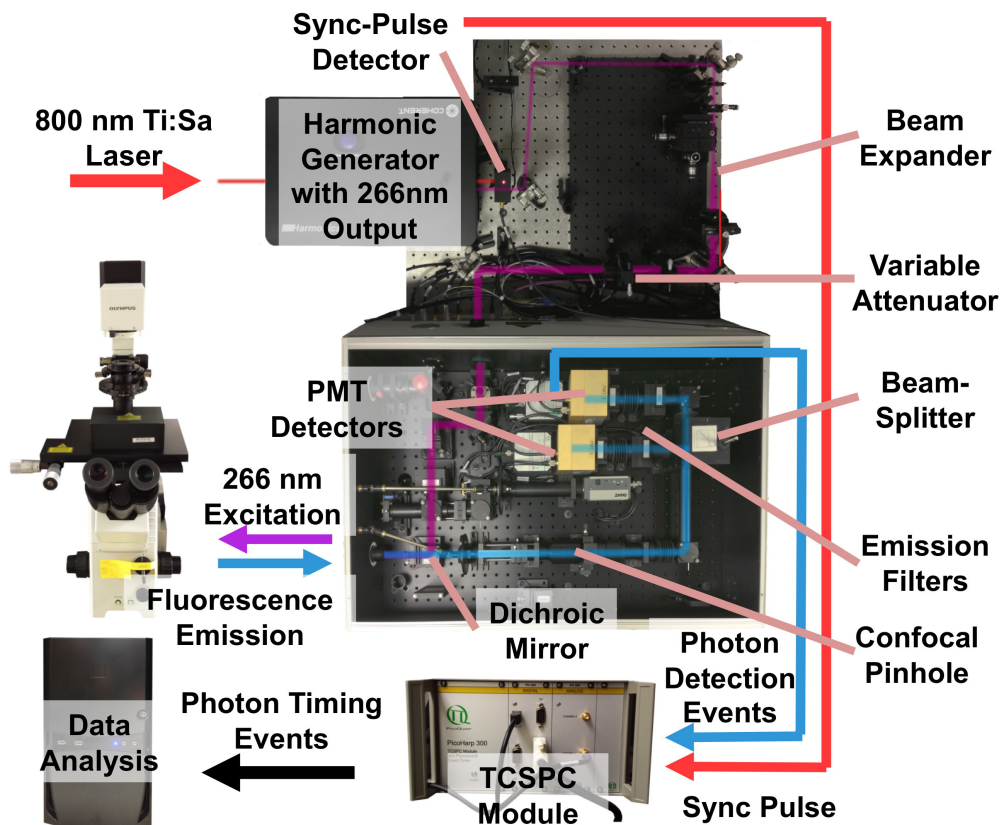

Figure S3: Fluorescence lifetime setup.

1.3 Lifetime measurement

Figure.S4 show the instrument response function (IRF), photon arrival histograms, fitted curve and residue for p-terphenyl at three Mg nanoapertures with different diameters. The IRF was measured by using the reflection of the incident light pulses from an unpatterned region of the samples, and replacing the bandpass filter with a neutral density filter. The

FWHM is about 156 ps. The SymPhoTime 64 software uses a multi-exponential reconvolution model to fit the TCSPC histograms. We fitted with a single time constant. Figure.S4 (a) are from an aperture with designed diameter 40 nm, dose 30 μs; The fitted single exponential constant is 0.13 ns which corresponds to the highest lifetime reduction ~7.2×. Figure. S4 (b) are from an aperture with designed diameter 50 nm, dose 20 μs; The fitted single exponential constant is 0.17 ns which corresponds to the highest lifetime reduction ~5.6× for diameter 50 nm aperture. Figure.S4 (c) are from an aperture with designed diameter 60 nm, dose 20 μs; The fitted single exponential constant is 0.27 ns which corresponds to the highest lifetime reduction ~3.5× for diameter 60 nm aperture.
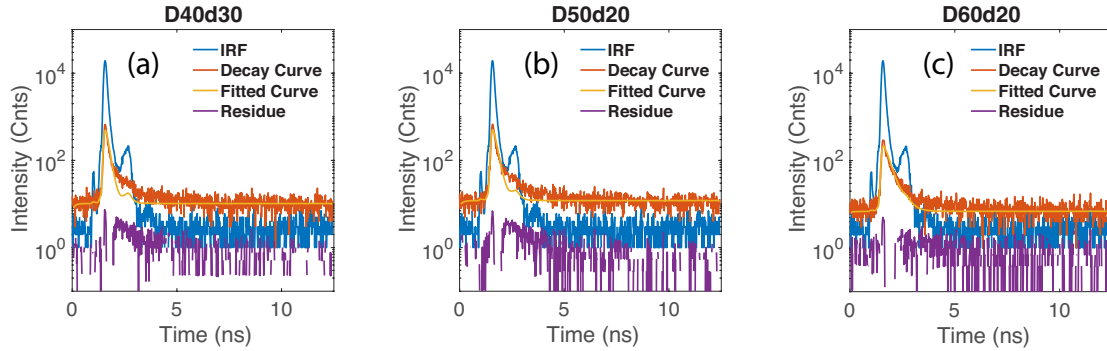

Figure S4: (a) The instrument response function (IRF), photon arrival histograms, fitted curve and residue for p-terphenyl at a Mg aperture with diameter 40 nm and dose 30 μs. (b) The instrument response function (IRF), photon arrival histograms, fitted curve and residue for p-terphenyl at a Mg aperture with diameter 50 nm and dose 20 μs. (c)The instrument response function (IRF), photon arrival histograms, fitted curve and residue for p-terphenyl at a Mg aperture with diameter 60 nm and dose 20 μs.

1.4   Count rate measurement results

Figure.S5(a) and (c) shows the measured normalized fluorescence count rate for Mg and Al nanoapertures. In fig.S5(b) and (d), simulated normalized NE (for a single emitter) is normalized by the NE without the metallic film. In the experiments, however, we don't know the number of molecules residing within the observation volume, so we cannot perform the same normalization. As a result, we perform the following normalization on the measured

count rate

$$normalized\_count\_rate = \frac{(Count\_rate - Bkg)}{(Volume \times Input\_power \times Const)} \tag{1}$$

,where Const is $2.5 \times 10^{-9}(KHZ/(m \times Joule))$, such that we can qualitatively examine experimental count rate versus undercut and aperture diameter, and compare to calculated results. Volume of each aperture is calculated using diameter and undercut plotted in fig. S1. From fig.S5, for both Mg and Al nanoapertures, the normalized count rate increases with increasing undercut and diameter, while the dependence on diameter become less evident when the diameter gets smaller, again, likely due to the low count rates observed.
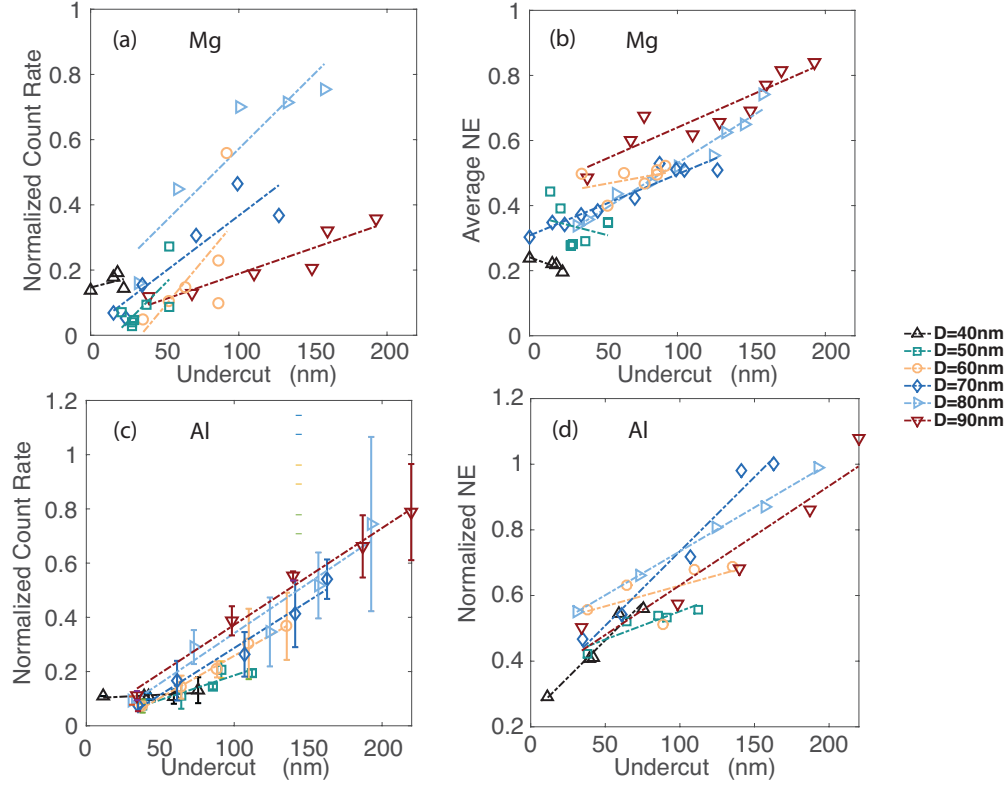

Figure S5: (a) Experimental normalized count rate from Mg nanoapertures plotted versus undercut. Each symbol represent different diameters. (b) Simulated net enhancement from Mg nanoapertures. Dashed lines are fitted using linear regression. (c) Experimental normalized count rate from Al nanoapertures plotted versus undercut. (d) Simulated net enhancement from Al nanoapertures.

2 Simulations

From fig.S6 to fig.S10, amplitudes of electric field $[E]^2$ upon planar wave excitation (λ 270nm) are plotted in x-z plane across the center of the apertures (y=0). The excitation is from the bottom of the aperture (z<0) and the unit of axis is in meter. Dashed lines are outline of the interface of metal and dielectric. Figure.S6 is from Al cylindrical nanoaperture with two diameters 60 nm and 92 nm and undercut 0 nm and 50 nm to compare the field distribution at different diameter and undercut. Consistent with discussion in the main manuscript, for Al cylindrical nanoapertures, field enhancement is localized at metal-dielectric interface and does not change with undercut depth for excitation enhancement. With increasing diameter, the excitation enhancement is reduced and the enhancement peak is shifted toward the center of the apertures. Figure.S7 is from Mg cylindrical nanoaperture with two diameters 40 nm and 92 nm and undercut 0 nm and 50 nm to compare the field distribution at different diameter and undercut. Consistent with discussion in the main manuscript, for Mg cylindrical nanoapertures, field enhancement is not localized at metal-dielectric interface but shift toward the center of the apertures due to excitation of waveguide mode. With increasing diameter, the excitation enhancement is reduced and the enhancement peak is further shifted toward the center of the apertures.

For fig.S8 and fig.S9, the nanoapertures are tapered conical shape with undercuts in parabola shape. The dimensions for each aperture are listed in table.1 and they are selected based on their average actual diameter (the mean of top and bottom diameter) for comparison. In fig.S8, (a) is an Al aperture with average diameter 76.5 nm and undercut 39.1 nm, similar in diameter but different in undercut with (b) which is an aperture with average diameter 78.7 nm, undercut 64.2 nm. In fig.S8 (c) is an Al aperture with average diameter 61.8 nm and undercut 38 nm, similar in undercut but different in diameter with (a) which is an aperture with diameter 76.5 nm, undercut 39.1 nm. In fig.S9, (a) is a Mg aperture with average diameter 81.8 nm and undercut 0 nm, similar in diameter but different in undercut with (b) which is an aperture with average diameter 80.8 nm, undercut 78.2 nm. In fig.S9 (c)

is a Mg aperture with average diameter 39.8 nm and undercut 0 nm, similar in undercut but different in diameter with (a) which is an aperture with diameter 81.8 nm, undercut 0 nm. Similar to cylindrical nanoaperture, larger diameter (especially bottom diameter) shifts the excitation enhancement peak away from the metal-dielectric interface towards the center of the apertures for both Al and Mg conical nanoapertures.

To compare conical shaped aperture with cylindrical shaped aperture, fig.S10 plot 2D near field of Al and Mg apertures with similar diameter and undercut. In fig.S10(a) is an Al cylindrical aperture with diameter 60 nm and undercut 50 nm, similar in diameter and undercut with (b), which is an Al conical nanoaperture with dimension 'al3', average diameter 61.8 nm, undercut 38 nm. In fig.S10(c) is an Mg cylindrical aperture with diameter 40 nm and undercut 0 nm, similar in diameter and undercut with (d), which is an Mg conical nanoaperture with dimension 'mg3', average diameter 42.9 nm, undercut 0 nm. The tapered conical shape aperture shifts excitation enhancement peak further towards the center of the aperture compared to its cylindrical shaped counterpart and the peak intensity is mostly determined by the bottom diameter.

Table 1: Dimensions of Mg and Al conical nanoapertures. 'TopD' stands for top diameter, 'Bdia' stands for bottom diameter, 'UC' stands for undercut, 'AveD' stands for average diameter (mean of top and bottom diameter) and 'DesignedD' stands for designed diameter.

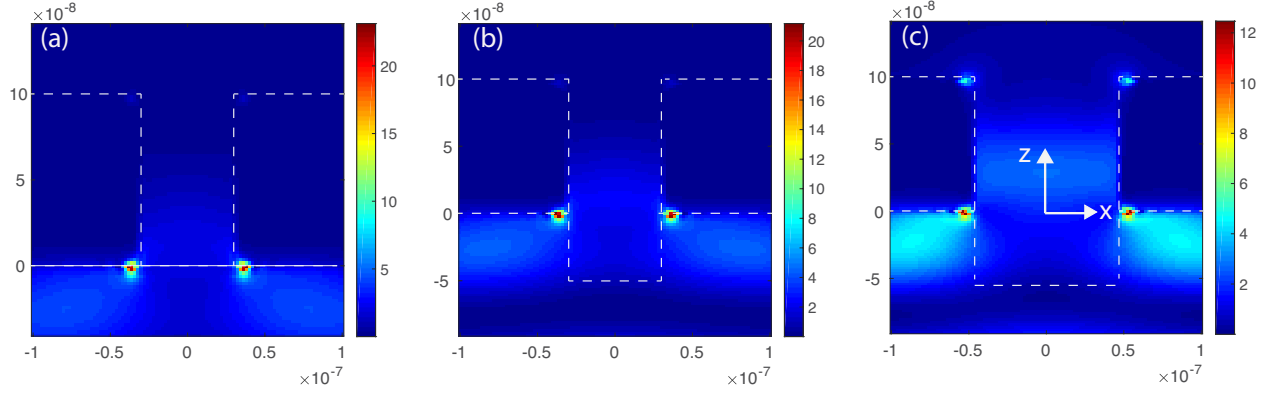| nm	TopD	Bdia	UC	AveD	DesignedD
al1	75.3	48.3	39.1	76.5	40
al2	96.7	60.7	64.2	78.7	50
al3	90	63	38	61.8	60
mg1	106.9	56.6	0	106.9	70
mg2	101.7	60.0	78.2	101.7	60
mg3	42.9	36.6	0	42.9	40

Figure S6: (a) 2D near field plot of excitation enhancement for Al cylindrical nanoaperture with diameter 60 nm, undercut 0 nm. (b) 2D near field plot of excitation enhancement for Al cylindrical nanoaperture with diameter 60 nm, undercut 50 nm. (c) 2D near field plot of excitation enhancement for Al cylindrical nanoaperture with diameter 92 nm, undercut 50 nm.
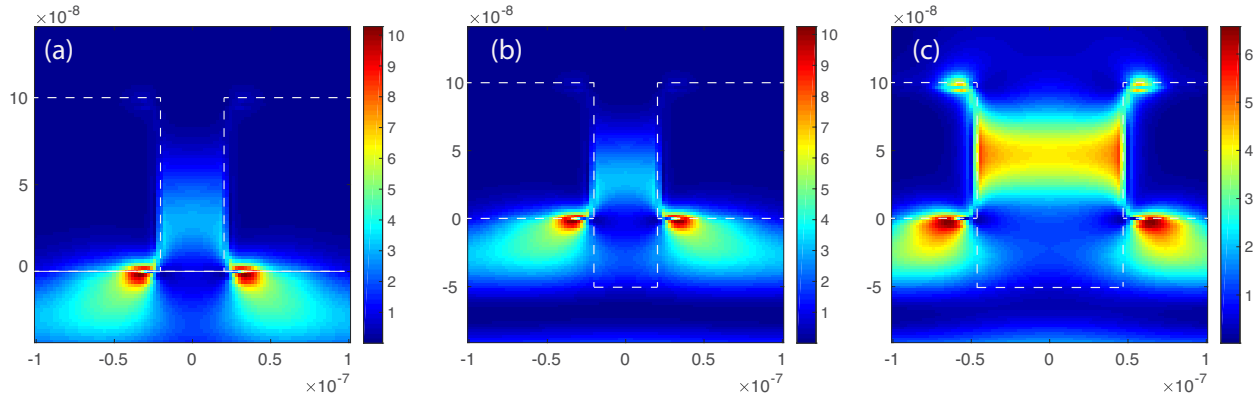

Figure S7: (a) 2D near field plot of excitation enhancement for Mg cylindrical nanoaperture with diameter 40 nm, undercut 0 nm. (b) 2D near field plot of excitation enhancement for Mg cylindrical nanoaperture with diameter 40 nm, undercut 50 nm. (c) 2D near field plot of excitation enhancement for Mg cylindrical nanoaperture with diameter 92 nm, undercut 50 nm.
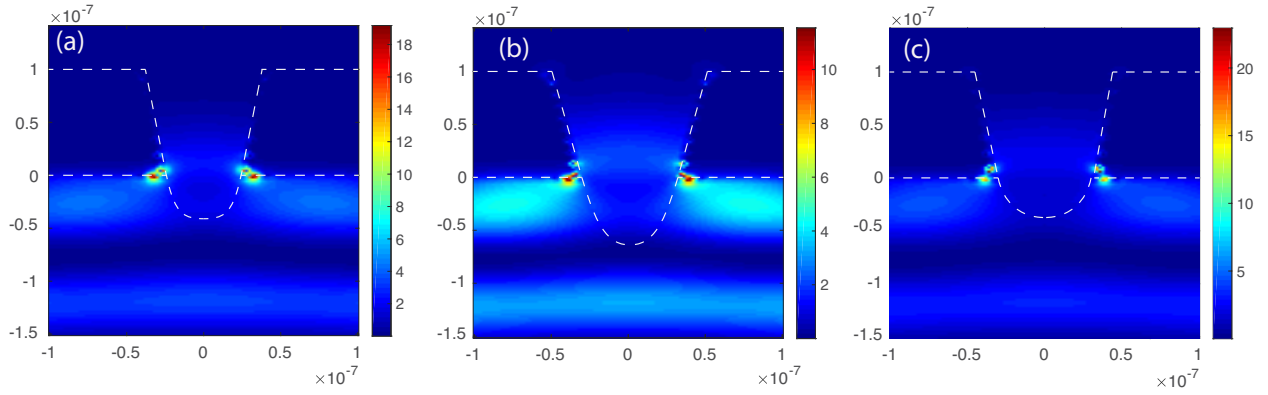
Figure S8: (a) 2D near field plot of excitation enhancement for Al conical nanoaperture with dimension 'al1' . (b) 2D near field plot of excitation enhancement for Al conical nanoaperture with dimension 'al2'.(c) 2D near field plot of excitation enhancement for Al conical nanoaperture with dimension 'al3'.
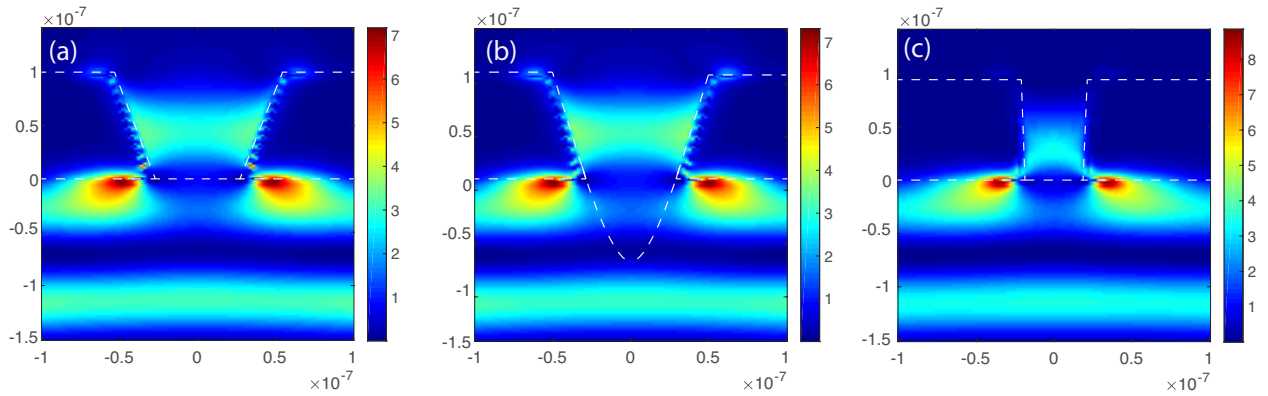

Figure S9: (a) 2D near field plot of excitation enhancement for Mg conical nanoaperture with dimension 'mg1' . (b) 2D near field plot of excitation enhancement for Mg conical nanoaperture with dimension 'mg2'.(c) 2D near field plot of excitation enhancement for Mg conical nanoaperture with dimension 'mg3'.
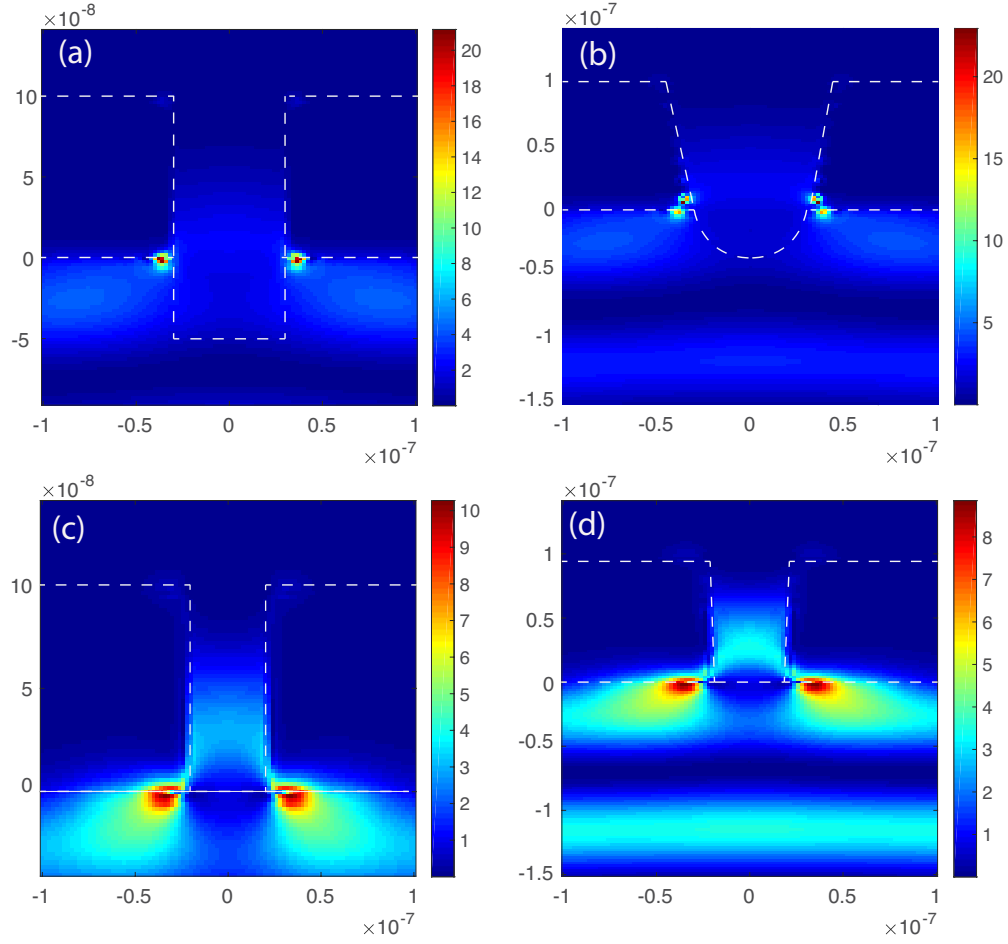
Figure S10: (a) 2D near field plot of excitation enhancement for Al cylindrical nanoaperture with diameter 60 nm, undercut 50 nm. (b) 2D near field plot of excitation enhancement for Al conical nanoaperture with dimension 'al3'.(c) 2D near field plot of excitation enhancement for Mg cylindrical nanoaperture with diameter 40 nm, undercut 0 nm. (d)2D near field plot of excitation enhancement for Mg conical nanoaperture with dimension 'mg3'.